Colloid Polym Sci 277:2–14 (1999)

LEADING CONTRIBUTION

R. Pelster
U. Simon

Nanodispersions of conducting particles: preparation, microstructure and dielectric properties

Received: 4 June 1998
Accepted: 18 August 1998

R. Pelster (✉)
II. Physikalisches Institut der Universität
zu Köln, Zülpicher Strasse 77,
D-50937 Cologne, Germany
e-mail: rolf@obelix.ph2.uni-koeln.de
Tel.: +49-221-4704986
Fax: +49-221-4702980

U. Simon
Institut für Anorganische Chemie
Festkörperchemie, Universität-GH Essen
Schützenbahn 70, D-45127 Essen, Germany

Abstract The properties of nanodispersions depend sensitively on their microstructure. Precise preparation techniques are needed to ensure controlled and well-defined spatial distribution of particles. We report on the correlation between synthesis, microstructure and dielectric properties. We conclude that temperature-dependent broadband dielectric spectroscopy up to microwave frequencies allows an insight into the microstructure of nanodispersions.

Key words Nanoparticles – Nanodispersion – Permittivity – Conductivity – Polarization

Introduction

In the last few years metal and semiconductor particles of nanometre size have become objects of rapidly growing interest [1–4]. The smallest nanoparticles constitute an intermediate state between bulk and molecular behaviour. They consist of tens of atoms up to a few thousand atoms, so quantization of the density of states becomes noticable [5–8]. The unique surface and electronic properties lead to a variety of chemical and physical applications, for example, in catalysis, optoelectronics, microelectronics, etc. Besides single particle characteristics the microstructure of nanodispersions is also of importance. Some applications require materials with well-separated particles, for example, for low-loss capacitive devices. Others, such as electromagnetic absorbers, need paths of agglomerating particles for energy dissipation. Figure 1 displays a schematic drawing of systems with different degrees of order: ordered, random and disordered nonrandom. Dispersions of nanoparticles differ from classical colloidal dispersions by a much smaller mean interparticle spacing s, which is therefore much more difficult to control. For example, consider a hexagonal lattice of particles with diameter d (see Fig. 2). The volume filling factor, $f = V_{\text{particles}}/V_{\text{total}}$, is

$$f = f_c \left(\frac{d}{d+s} \right)^3 , \tag{1}$$

where $f_c = \sqrt{2}\pi/6 \simeq 0.74$ corresponds to the highest packing density where $s = 0$ (fcc or hcp lattice). At constant f the interparticle distance scales with the particle size: $s = d[(f_c/f)^{1/3} - 1]$. For Au_{55} particles, for example, $d = 1.4$ nm [1] and filling factors in the range from 2 to 20% correspond to spacings of $s = 3.3$–0.4 nm. A small displacement of the particles on a scale of a few angstroms would change the degree of order (see Fig. 1). Interactions between particles cannot be neglected either, since even at spacings of a few nanometres charge transport via hopping may occur: this strongly depends on the exact value of s. It is obvious that a distribution of particle sizes induces a distribution of interparticle spacings and thus has an effect on the degree of order. Therefore, the preparation of well-defined systems

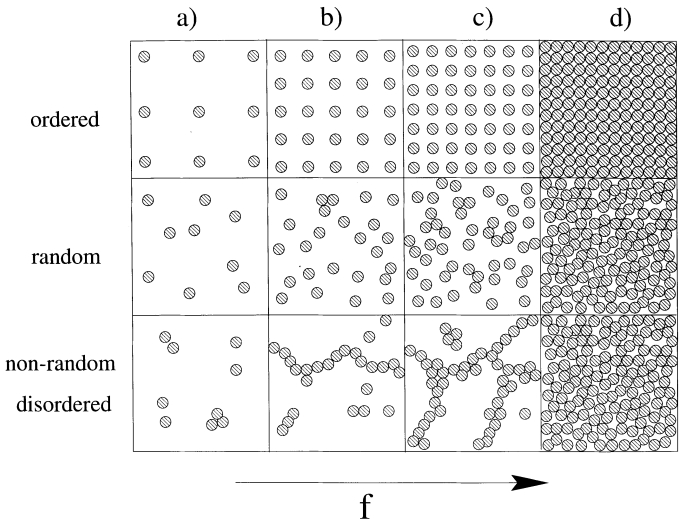

Fig. 1a–d Particle distribution in ordered, random, and disordered nonrandom systems at different filling factors f

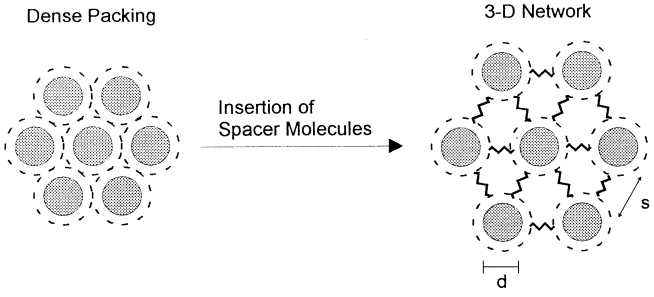

Fig. 2 3D network of ligand-stabilized nanoparticles, where larger bifunctional molecules act as dielectric spacers [16]

requires good control of nucleation, particle growth and dispersion processes.

In this paper we discuss to what extent different preparation techniques allow the microstructure to be controlled. We show that microstructure and dielectric response are correlated, and so broadband dielectric spectroscopy yields information on both the microstructure of nanodispersions as well as on single particle properties. We consider metals, semiconductors and intrinsically conducting polymers.

Preparation of nanodispersions

The preparation of metal and semiconductor nanodispersions with a homogeneous dispersion of uniform particles is the goal of many preparative efforts. Obtaining samples with well-separated particles is far from trivial and becomes more difficult the higher the filling factor f. The kind of particle arrangement obtained depends on the preparation strategy for the particles, on the dispersion or embedding technique, as well as on the choice of the matrix (see Fig. 1). The various procedures for the synthesis of nanoparticles cover a broad field from purely physical methods, such as metal evaporation or electron beam techniques, to classical colloid-chemical or organometallic preparation techniques. The reduction of solvent metal ions or complexes by suitable reductive agents [9, 10] or by radiolytic or photochemical processes [11] belongs to the latter class. In general, bare nanoparticles have a very short lifetime due to their high reactivity. They can be stabilized by embedding them into suitable protecting matrices, such as glasses, polymers, micelles or porous solids. Another possibility is to cover their surface with charged molecules or ligands. This also prevents Ostwald ripening and agglomeration due to van der Waals forces. The effect of electrostatic and steric stabilization is explained in detail in Ref. [12]. A comprehensive review of preparation techniques would go beyond the scope of this paper, so we do not discuss techniques for granular metals, cermets or structurally related conducting polymer blends yielding a random or disordered distribution. We mainly focus on some common techniques which are known to control adequately particle size and dispersion.

Ligand stabilized nanoparticles

The preparation of ligand-stabilized metal or semiconductor nanoparticles is based on the classical routes of colloid or organometallic chemistry. Besides radiolytic and photochemical techniques two typical preparation methods are used (see Fig. 3): (1) for metals (usually

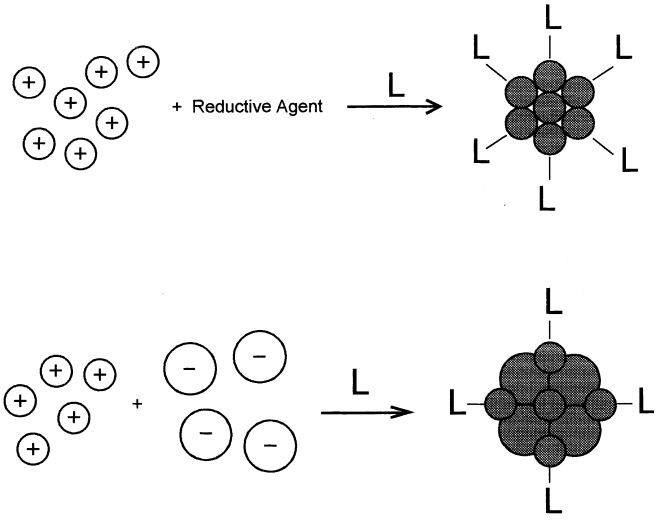

Fig. 3 a Formation of metal nanopartices by reduction of metal ions in the presence of ligands. **b** Formation of semiconductor nanoparticles by reaction of metal ions with group V–VII anions in the presence of ligands

transition metals) the reduction of soluble metal salts or complexes by suitable reductive agents, for example, hydrogen, diborane, methanole or citric acid, and (2) for semiconductors the reaction of metal ions or complexes with group V, VI or VII anions. In order to control the particle size typical colloid-chemical stabilizers or electron-donor ligands, such as phosphine or thiole are added. They saturate the free valences on the surface of the particles and lead to electrostatic or steric stabilization. The size, for which the nanoparticles are stable, is given by so-called magic numbers [1, 2, 4, 10]: the atoms tend to form close packed spheres, i.e. the central atom is surrounded by a shell of 12 nearest neighbours, which in turn is covered by a second shell of 42 atoms, etc. Examples of ligand-stabilized metal nanoparticles are $Au_{55}(PPh3)_{12}Cl_6$, $Pt_{309}phen{*}_{36}O_{30}$ or $Pd_{561}phen_{36}O_{200}$, where "phen$*$" denotes batho-phenanthroline and "phen" is 1, 10-phenanthroline. A comprehensive review of synthetic aspects, structure and characterization is given in Ref. [2].

Most of the materials are stable in air and can be compacted to solids (see Fig. 1 at high f). While the metal nanodispersions typically exhibit a dense but mostly disordered packing, semiconductor dispersions can even be crystallized in 3D superlattices by removing the solvent. Examples are $Cu_{20}Se_{13}(PR_3)_{12}$, $Cu_{146}Se_{73}(PPh_3)_{30}$, $Cd_{17}S_4(RS)_x$ and $Cd_{32}S_{14}(RS)_y$ [10, 13]. Although the metal or semiconductor nanoparticles are separated by the insulating molecules of the surrounding ligand shell, charge transport via hopping is possible [14]. Dispersions with lower filling factors are obtained by dissolving the ligand-stabilized particles and a polymer in a suitable solvent. However, the particles tend to aggregate and to form nucleation centres with superstructures [15]. In order to increase the interparticle spacing in a defined way, bifunctional organic molecules have been connected to ligand-stabilized metal nanoparticles [16, 17]. They act as dielectric spacers, so a 3D network is formed (see Fig. 2). We shall show later that electronic transport between neighbouring particles can be tailored chemically using spacer molecules of different lengths.

A more or less equidistant spatial separation of metal or semiconductor nanoparticles can also be realized using reverse micelles or block copolymer micelles [18] (see Fig. 4). They form in a selective solvent and serve as "nanoscopic reactors" for single particles. For this purpose a soluble metal salt is transferred to the core of the micelles. The nanoparticles are formed via reduction, the size of the nanoparticles depending both on the number of metal ions provided and on the size of the micelle. The micelles can be assembled to form defined films. Monolayers of Au nanoparticles ($d = 2$, 4, 5 or 6 nm) in polystyrene-block-polyethyleneoxide micelles show a rather regular hexagonal arrangement. The interparticle spacing is in the range of more than 10 nm

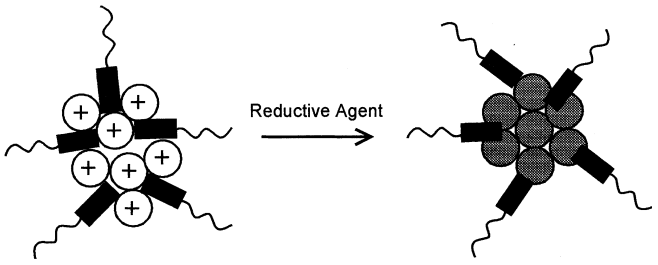

Fig. 4 Formation of a nanoparticles by reduction of metals in the core of a block copolymer micelle

and is expected to be large enough to exclude charge transport. However, the electrical properties of these fascinating nanoscaled arrays have not been reported up to now.

Nanoparticles in porous solids

Nanoparticles can also be prepared and stabilized in the confinement of porous solids with well-defined pore or channel structures. Transition metals, such as Pt, Pd, Ag and Ni, and semiconductors, such as PdS, CdS,CdSe and SnO_2, have been incorporated in the voids of molecular sieves, for example, in zeolites or related mesoporous phases [19–25]. The particles are synthesized either via an ion-exchange reaction or via decomposition of precursors.

In the first case the host acts as a solid electrolyte (see Fig. 5). The negative charges of the polyanionic zeolite lattice are compensated by monovalent mobile cations, usually by Na^+. In solution or in a melt they are exchanged for mono- or multivalent metal cations (transition or main group metals). These can be reduced by suitable agents, such as hydrogen or alkali metal vapour. Since the metal atoms are located on well-defined cation sites, the nanoparticles form via a migration and aggregation process.

A second method of synthesis consists of loading the dehydrated zeolite with organometallic precursors from the gas phase or from solution. Thermal treatment then

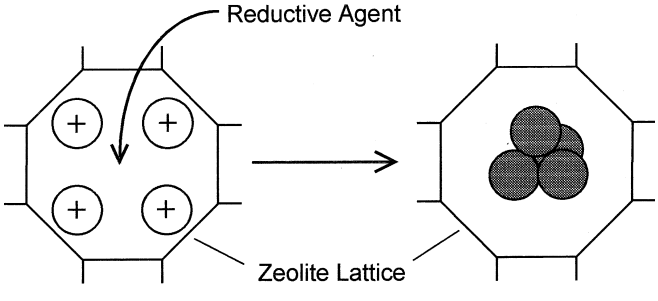

Fig. 5 Formation of nanoparticles in a zeolite matrix by reduction of transition metal ions with suitable reductive agents

leads to ligand desorption and decomposition, which enables the metal atoms to aggregate.

One might expect that the synthesis of nanoparticles in the confinement of crystalline host lattices results in monodisperse and ordered nanodispersions. However, in general it causes a local degradation of the host lattice, for example, by partial hydrolysis of the Si—O—Al or Si—O—Si bonds in the zeolite. Furthermore, this may also lead to the formation of nanoparticles or microcrystallites on the surface of the matrix [26]. Therefore, the effect of the matrix as a size and order controlling confinement is strongly reduced. The interparticle spacing is not well-defined and the size distributions of the nanoparticles are broader compared to those obtained for ligand stabilized particles or particles in block copolymers.

Nanoparticle synthesis by metal evaporation

Various metals, preferably volatile ones, can be thermally or electrically evaporated. A colloidal suspension is obtained by condensation of the metal vapour into a dispersing medium [12]. This simple and long-established method allows the trapping of metal and mixed-metal nanoparticles in different matrices such as frozen solvents or polymers [27]. A closely related method is the inert gas evaporation technique combined with a simultaneous plasma polymerisation process [28]. The particle size and the filling factor are experimentally controlled via the evaporation rate and the pressure. In general, the particles tend to agglomerate even at low filling factors. However, an extremely narrow size distribution and a homogeneous interparticle spacing are obtained when bifunctional spacer molecules are added to the matrix. Examples which refer to Fig. 1b and c (ordered) are given in Refs. [28, 29].

Microstructure and dielectric properties

The effective permittivity or dielectric function (DF) of a dispersion, $\varepsilon_{\text{eff}} = \varepsilon' - i\varepsilon''$, may be measured, for example, via the complex capacitance of a material-filled condenser cell: $C_{\text{mat}} = \varepsilon_{\text{eff}} \cdot C_0$, where C_0 denotes the capacitance of the empty cell. In general, ε_{eff} is a function of both the frequency ν and the temperature T. In the case of the dielectric heterostructures investigated here, its values depend on the permittivities of the matrix and particles, ε_m and ε_p, on the volume filling factor, $f = V_{\text{particles}}/V_{\text{total}}$, as well as on the form of the particles and on the microstructure of the material. In the following sections, we consider particles with sufficiently high conductivities, so that up to microwave frequencies the imaginary part of ε_p is governed by losses due to free-charge-carrier absorption, while the real part can be assumed to be independent of frequency: $\varepsilon_p = \varepsilon'_p - i\sigma_p/(\varepsilon_0\omega)$, where σ_p denotes the dc conductivity, $\varepsilon_0 = 8.854 \times 10^{-12}$ F/m, and $\omega = 2\pi\nu$. In addition, we assume the particle size d to be small compared to the wavelength so that there is no skin effect. This implies, for example, that $\nu < 100$ GHz for metal particles with $d = 200$ nm [$\nu_{\text{limit}} \propto 1/(\sigma_p d^2)$]. In this frequency range ε_{eff} is independent of d as long as no hopping transport takes place and ε_p shows no size-effects. We restrict ourselves to dispersions of dielectrically homogeneous particles. However, we shall discuss the influence of contact resistance. In a homogeneous electric field the dispersed particles become polarized, and dipole as well as multipole fields are induced. The dipole-dipole interaction in 3D is long-range and each particle is exposed to the superposition of the external field and the fields induced by the surrounding particles. The higher the filling factor, the more important the spatial distribution of the particles. In order to illustrate this effect, we first consider the limit of low filling factors, where structural aspects are neglected.

Dilute systems

In ordered or random dilute systems of nonagglomerating particles the distances between the particles are large, so the local field acting on each particle is approximately uniform. In spheres or oriented ellipsoids only dipole moments are induced. For such dispersions of particles in a continuous matrix (matrix-inclusion topology, see Fig. 1a) the Maxwell-Garnett (-Sillars) formula holds [30, 31]:

$$\varepsilon_{\text{eff}}(\omega) = \varepsilon_m \cdot \left(1 + \frac{1}{A}\frac{fx}{1 - fx}\right) \quad \text{for} \quad f|x| \ll 1, \tag{2}$$

where

$$x = \frac{A(\varepsilon_p - \varepsilon_m)}{\varepsilon_m + A(\varepsilon_p - \varepsilon_m)}. \tag{3}$$

The depolarization factor A depends on the form of the particle: for spheres $A = 1/3$. The limits $A = 1$ and $A = 0$ correspond to parallel layers having an orientation perpendicular or parallel to the applied field (see Fig. 6). In these cases, the system reduces to a simple series or parallel circuit and Eq. (2) is exact for all f. For $A > 0$ charge accumulation at the interfaces between the different materials causes a polarization process with a maximum $\text{Im}[\varepsilon_{\text{eff}}]$ at the relaxation frequency $\nu_{\text{relax}} = (2\pi\tau)^{-1}$ (see Fig. 7a). Inserting the generalized permittivities of particles and matrix, $\varepsilon_p = \varepsilon'_p - i\sigma_p/(\varepsilon_0\omega)$ and $\varepsilon_m = \varepsilon'_m - i\sigma_m/(\varepsilon_0\omega)$, yields the Maxwell-Wagner-Sillars formula

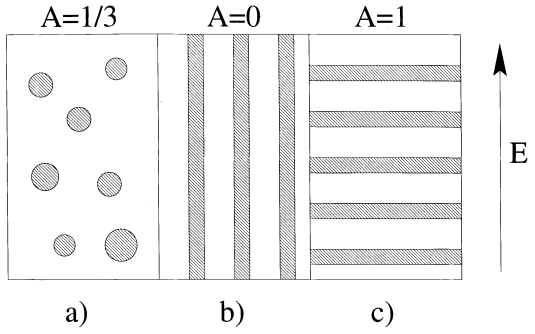

Fig. 6 **a** Dispersed spherical particles ($A = 1/3$) and **b** multilayer systems with orientation parallel ($A = 0$, parallel circuit) or perpendicular ($A = 1$, series circuit) to the applied field. An interfacial polarization process only occurs for $A > 0$ ($\Delta\varepsilon > 0$, see Eqs. 4 and 5)

$$\varepsilon_{\text{eff}}(\omega) = \varepsilon_\infty + \frac{\Delta\varepsilon}{1 + i\omega\tau} - i\frac{\sigma_{dc}}{\varepsilon_0\omega}. \tag{4}$$

The relaxation strength $\Delta\varepsilon$, effective conductivity σ_{dc}, high-frequency permittivity ε_∞ and relaxation time τ are [30, 31]

$$\Delta\varepsilon = A\frac{(\varepsilon'_m\sigma_p - \varepsilon'_p\sigma_m)^2 f(1-f)}{[\varepsilon'_m + A(1-f)(\varepsilon'_p - \varepsilon'_m)][\sigma_m + A(1-f)(\sigma_p - \sigma_m)]^2}, \tag{5}$$

$$\varepsilon_\infty = \varepsilon'_m\left(1 + f\frac{\varepsilon'_p - \varepsilon'_m}{\varepsilon'_m + A(1-f)(\varepsilon'_p - \varepsilon'_m)}\right), \tag{6}$$

$$\sigma_{\text{dc}} = \sigma_m\left(1 + f\frac{\sigma_p - \sigma_m}{\sigma_m + A(1-f)(\sigma_p - \sigma_m)}\right), \tag{7}$$

$$\tau = \varepsilon_0\frac{\varepsilon'_m + A(1-f)(\varepsilon'_p - \varepsilon'_m)}{\sigma_m + A(1-f)(\sigma_p - \sigma_m)}. \tag{8}$$

Let us consider the important case of highly conducting particles, so that $\sigma_m/(\sigma_p - \sigma_m) \ll A(1-f)$ and $\varepsilon_m\sigma_p \gg \varepsilon_p\sigma_m$. The polarization of the particles yields an enhancement of the static permittivity $\varepsilon_s = \varepsilon'_{\text{eff}}(\omega\tau \ll 1) = \Delta\varepsilon + \varepsilon_\infty$ compared to the matrix value ε_m (see Fig. 7b). With increasing filling factor the mean interparticle distance decreases, i.e. the interparticle capacitance increases and so does ε_s. ε_s is obtained directly from Eq. (2) with $x = 1$, i.e. at low frequencies conductive particles behave as if they had a real permittivity $\varepsilon_p = \infty$ (see Eq. 3). The smallest particles exhibit a reduced electronic polarizability, so ε_p becomes finite and size dependent [32]. This results in a small correction ($x < 1$ instead of $x = 1$), an effect we neglect in the following treatment. The effective dc conductivity is governed by the higher resistances, i.e. by the matrix material:

$$\sigma_{\text{dc}} = \sigma_m\left(1 + \frac{f}{A(1-f)}\right). \tag{9}$$

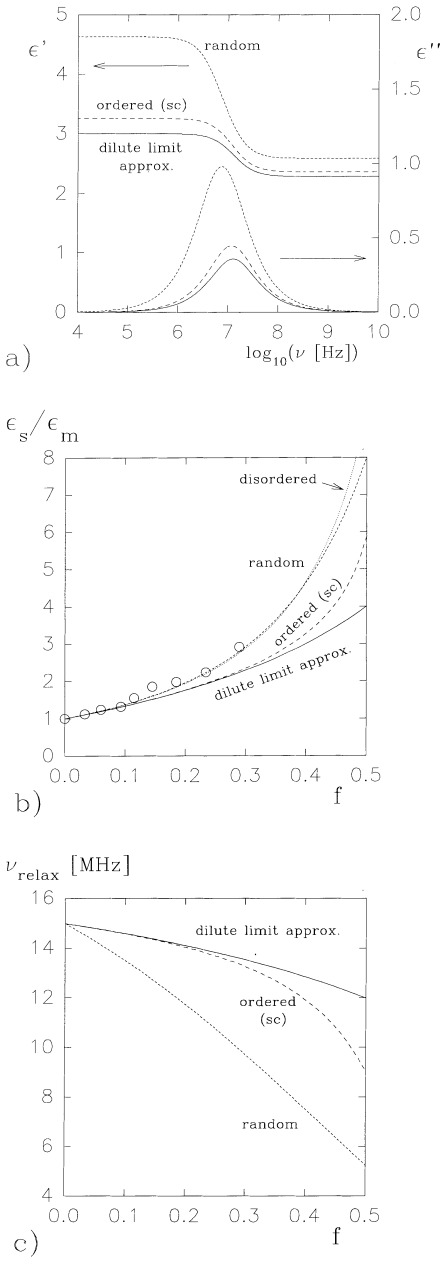

Fig 7a–c Interfacial polarization process for matrix inclusion topology of well-separated conducting spheres embedded in an insulating matrix ($\varepsilon'_p = 10$, $\sigma_p = 0.01$ S/m, $A = 1/3$, $f = 0.4$, $\varepsilon'_m = 1$, $\sigma_m = 0$). **a** Permittivity $\varepsilon_{\text{eff}} = \varepsilon' - i\varepsilon''$ vs frequency ν in a semilog plot. **b** Static permittivity ε_s and **c** relaxation frequency $\nu_{\text{relax}} = 1/(2\pi\tau)$ vs filling factor f. Dilute limit approximation: Eqs. (2)–(8); ordered: Eq. (12) for the simple cubic lattice; random: numerical analysis of the Hanai-Bruggeman formula Eq. (14); disordered: effective cluster model, Eq. (2) with x from Eq. (18). Since the ratio $\varepsilon_s/\varepsilon_m$ only depends on f, we also compare with data for conductive nanodroplets of water in butyl rubber ($d \simeq 4$–6 nm, $T = 20$ °C [41])

σ_{dc}, ε_s, ε_∞ and $\Delta\varepsilon$ are independent of the particle conductivity; however, σ_p determines the relaxation frequency, $\nu_{\text{relax}} = (2\pi\tau)^{-1} \propto \sigma_p$. Combining Eqs. (5) and (8) yields

$$\sigma_p = \frac{\varepsilon_0 \Delta\varepsilon}{\tau}\frac{\gamma}{f}, \tag{10}$$

where $\gamma = [1 + A(1-f)(\varepsilon'_p/\varepsilon'_m - 1)]^2$. The relaxation frequency decreases with increasing filling factor (see Fig. 7c) and lies above

$$\nu_{\text{relax}} \geq \frac{A(1-f)\sigma_p}{2\pi\varepsilon_0 \max\{\varepsilon'_p, \varepsilon'_m\}} = \frac{A(1-f)\sigma_p\ [\text{S/m}]}{\max\{\varepsilon'_p, \varepsilon'_m\}} \times (1.8 \times 10^{10}) \quad [\text{Hz}] \tag{11}$$

(see Eq. 8). For particle conductivities higher than 10 S/m only the static permittivity ε_s (Eq. 2 with $x = 1$) and a possible dc conductivity (Eq. 9) are observed up to the microwave region. According to Eq. (11) high-frequency measurements are required in order to determine the dc conductivity of dispersed particles (via Eq. 8 or 10).

Effect of particle interaction

The above equations can only be used as a rough estimate to predict the relaxation frequency of well-separated particles or to evaluate their conductivity. Only in the limits $A = 0$ and $A = 1$, i.e. for a parallel or series circuit of layers (Fig. 6) are they exact even at high filling factors. In general, higher multipoles have to be taken into account, since the local field acting on each particle is nonuniform. This implies that spatial distribution of the particles is involved.

First, we focus on ordered systems (see Fig. 1). For a cubic lattice (sc) of spherical particles ($A = 1/3$) Eq. (2) has been extended to include effects of multipoles up to $n = 7$ [33]. It can be written in the form

$$\varepsilon_{\text{eff}}(\omega) = \varepsilon_m\left(1 + 3\frac{fx}{1 - fx(1+M)}\right) \text{ for } f \leq 0.46, \tag{12}$$

with

$$M = b_1 x_5 f^{11/3} + c_1 x_7 f^5 - a f^{7/3}\frac{1 + c_2 x_5 f^{11/3} + c_3 x_5^2 f^{22/3}}{-x_3^{-1} + b_2 f^{7/3} + c_4 x_5 f^6}$$

and $x_n = (\varepsilon_p - \varepsilon_m)/[\varepsilon_p + (n+1)/n \cdot \varepsilon_m]$. The coefficients are $a = 1.3045$, $b_1 = 0.01479$, $b_2 = 0.4054$, $c_1 = 0.1259$, $c_2 = 0.5289$, $c_3 = 0.06993$ and $c_4 = 6.1673$. Precise numerical calculations including all higher multipole moments have been carried out [33, 34]. In the limit $x = 1$, i.e. for the static permittivity of conducting particles dispersed in an insulating matrix, a simple interpolation formula holds [34]:

$$\varepsilon_s(x = 1) = \varepsilon'_m[1 - \pi/2 \ln(1 - f/f_c)] \text{ for } f \leq f_c, \tag{13}$$

where $f_c = \pi/6$ is the percolation threshold at which the metallic spheres touch. For $f \leq 0.25$ this equation also describes bcc and fcc lattices with an accuracy better than 1% [34]. The effective permittivity of a dispersion according to Eqs. (2) and (12) is compared in Fig. 7. The effects of higher multipole moments are an enhancement of the real and imaginary parts of ε_{eff}, i.e. of both energy storage and loss, and a decrease of the relaxation frequency. The deviations from the dilute-limit approximation become visible above $f \simeq 0.2$. Note that at high frequencies or for nonmetallic inclusions ($x < 1$) the deviations from Eq. (2) are smaller (for different lattices and particle shapes we refer to Refs. [34–37]).

While in ordered systems the spacing between particles is fixed, in random or disordered systems there are also close-packed particles which form secondary aggregates. Therefore, the deviation from Eq. (2) is expected to be seen at much lower filling factors. There is a variety of approximative mean-field mixture formulas for random systems (for reviews see Refs. [30, 31]). The higher multipole moments are not calculated explicitly but each particle is assumed to be polarized in a (modified) homogeneous field. In general, two topologies are considered [38, 39]: (1) matrix inclusion systems, where particles are dispersed in a continuous medium (e.g. suspensions, emulsions, filled polymers or nanoparticles in porous solids) and (2) aggregate topology systems, where two topologically equivalent materials are mixed on a random base (e.g. compact powders, interpenetrating network structures or heterogeneous polymer mixtures). Often the dependence of experimental ε_{eff} data on the filling factor or temperature can be used to check whether a mixture formula is applicable to a system. As before (Eqs. 2 and 12) we concentrate on the matrix inclusion topology. One of the formulas proposed for random systems is the Hanai-Bruggeman formula, where the higher concentration of spheres is taken into account using an integral method [30, 31]:

$$(1-f)^3\ \frac{\varepsilon_{\text{eff}}}{\varepsilon_m} = \left(\frac{\varepsilon_{\text{eff}} - \varepsilon_p}{\varepsilon_m - \varepsilon_p}\right)^3 \text{ for } f < f_c. \tag{14}$$

The frequency dependence of ε_{eff} is displayed in Fig. 7a. Expanding the right-hand term $(1 - 3\varepsilon_{\text{eff}}/\varepsilon_p + 3\varepsilon_m/\varepsilon_p + \cdots)$ yields

$$\varepsilon_{\text{eff}}(\omega) \simeq \varepsilon_m \frac{1 + 3(\varepsilon_m/\varepsilon_p)}{(1-f)^3 + 3(\varepsilon_m/\varepsilon_p)} \text{ for } |\varepsilon_{\text{eff}}|, |\varepsilon_m| \ll |\varepsilon_p|. \tag{15}$$

Equation (15) takes the form of the interfacial polarization process, Eq. (4), when we insert the permittivity of conducting particles and of an insulating matrix, $\varepsilon_p = \varepsilon'_p - i\sigma/(\varepsilon_0\omega)$ and $\varepsilon_m = \varepsilon'_m$. Now $\sigma_{\text{dc}} = 0$ and

$$\tau \simeq \varepsilon_0 \cdot \frac{\varepsilon'_m + (1/3)(1-f)^3\varepsilon'_p}{(1/3)(1-f)^3\sigma_p} \quad (16)$$

instead of Eq. (8). Eq. (10) remains valid replacing γ by $\overline{\gamma} \simeq [1 + 1/3 \cdot (1-f)^3\varepsilon'_p/\varepsilon'_m]^2/(1-f+f^2/3)$. Figure 7b displays the static permittivity

$$\varepsilon_s = \frac{\varepsilon_m}{(1-f)^3} \quad (17)$$

(see Eqs. 14 or 15 for $|\varepsilon_p| \to \infty$). Above $f = 0.1$ a deviation from the dilute limit, Eq. (2) becomes visible. The effects of particle interaction are qualitatively the same as for ordered systems but more intense, i.e. the ε_{eff} values are enhanced and the relaxation is shifted to lower frequencies (Fig. 7c). In addition, the half-width of the relaxation peak in Fig. 7a is about 5% larger than that of the Debye form, Eq. (4). Figure 7b also shows values for conductive nanodroplets of water in butyl rubber ($d = 4$–6 nm) [41]. The random dispersion is well-described by Eq. (17). For $T = 25°\text{C}$ and $f = 0.22$, the interfacial polarization process is observed at $\nu_{\text{relax}} = 160$ MHz [42]. This allows the determination of the droplet conductivity, which is due to an unknown quantity of dissolved ionic impurities. With $\varepsilon_p \simeq 80$ and $\varepsilon_m = 2.3$, Eq. (16) yields $\sigma_p \simeq 0.84$ S/m.

In the size range below 1 μm secondary aggregates, i.e. agglomerating particles, form easily due to van der Waals forces (see Fig. 1). A nonrandom, disordered suspension of equally sized metallic spheres in an insulating matrix has been described in the effective cluster model of Doyle [40]. A fraction f/f_c of the particles is assumed to form random close-packed spherical clusters of arbitrary size. Multipole interactions within the clusters are taken into account while interactions between clusters and isolated spheres are treated in a dipole approximation. The static permittivity ε_s is given by Eq. (2) with $A = 1/3$, whereas the simple dipole approximation $x = 1$ is to be replaced by

$$x = 1 + (f/f_c) \cdot (1/f_c - 1) \text{ with } f_c \simeq 0.63. \quad (18)$$

Up to $f = 0.4$ there is no noticable difference to the Hanai-Bruggeman result (see Fig. 7b), but approaching f_c larger values are obtained.

In general, the increase of ε_{eff} and the lowering of the relaxation frequency depend on the exact spatial distribution of the particles and become more pronounced with increasing degree of agglomeration. In addition, agglomeration gives rise to a broadening of the relaxation peak [43]. Precise numerical techniques are described in Refs. [43–45] (matrix inclusion topology for $f < f_c$) and in Refs. [46, 47] (aggregate topology for $|\varepsilon_p| \leq 100$, i.e. for $\nu > \nu_{\text{relax}}$ [48]).

Detecting agglomeration

As we have seen above, the relaxation frequency of well-separated highly conducting particles with $\sigma_p > 10$ S/m lies far above the gigahertz range (Eq. 11). Only the quasistatic permittivity should be observed at lower frequencies. If losses are observed, they may be due to the matrix or to charge transport between neighbouring particles. Here we are going to use the latter case as a criterion for agglomeration. As long as no dc conductivity is observed, any change of the relaxation frequency, its temperature dependence, and the form of the loss peak may hint at agglomeration. Agglomerating particles with contact resistances in-between can be considered as clusters of reduced conductivity $\sigma_{\text{cluster}} < \sigma_p$. The same holds for particles which are separated by very thin barriers so that charge hopping occurs (see next section). The Maxwell-Wagner-Sillars process of such clusters is observed at lower frequencies, $\nu_{\text{relax}} \propto \sigma_{\text{cluster}}$ (see Eq. 10), and may exhibit an altered temperature dependence.

The dependence of the interfacial polarization process on the particle or cluster conductivity also allows chemical reactions to be monitored. For example, SnO_2 particles in a porous zeolite matrix can serve as gas sensors [49]. The particles with $d = 2$–4 nm form secondary aggregates of 20–40 nm. Switching between oxidative and reductive gas environments results in a reversible chemical reaction. It alters the conductivity within these particle agglomerates and thus both the relaxation frequency and the effective ac conductivity. This induces a strong change of ε_{eff} that may be monitored by an electronic device.

Agglomeration also affects the shape of the polarization process. Figure 8a displays the permittivity of TiC particles dispersed in a plaster matrix [50]. At room temperature TiC exhibits a bulk conductivity of $\sigma_p \simeq 1.7 \cdot 10^6$ S/m. A strong frequency dependence is observed, which corresponds neither to Eq. (4) (for $\omega\tau > 1$) nor to a simple power law $\varepsilon \propto \omega^{-\alpha}$. Both the real and the imaginary part of the DF are enhanced compared to the values for the matrix. The enhancement of the real part is due to a polarization effect. There is no dc conductivity, but the increase of the imaginary part hints at a current flow in clusters. The interfacial polarization process seems to be shifted to very low frequencies and is spread out over a large frequency range. The ac conductivity of different systems with isolated, agglomerated and percolating particles is compared in Fig. 8b. Only the latter system exhibits dc conductivity. The agglomerated particles show an intermediate behaviour with a characteristic dispersion.

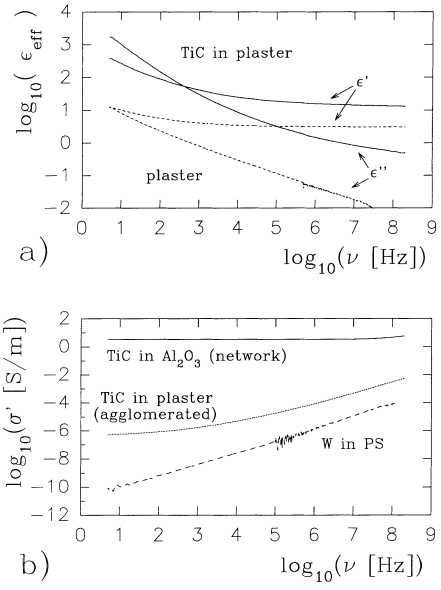

Fig. 8 **a** Permittivity ε_{eff} of a *TiC* particles in plaster vs. frequency ν in a double-log plot. *Solid lines*: mixture ($f = 0.18$, $d = 800$ nm), *dashed line*: plaster matrix. **b** Ac conductivity $\sigma = \varepsilon_0 \varepsilon'' \omega$ of isolated particles (W in polystrol (PS), $f = 0.11$, $d = 400$ nm), TiC particles in plaster (see **a**), and a percolating network of TiC particles (sintered TiC/Al_2O_3 mixture, $f = 0.17$, $d = 800$ nm) [50]

Hopping conductivity

Until now we have considered systems where there is no dc conductivity below f_c, unless the matrix itself is conducting. With the exception of the above-mentioned agglomeration effects, we have made the implicit assumption of an interparticle spacing s large enough to prevent charge transport. However, when conducting particles are separated by thin insulating barriers of the order of 1 nm, dc conduction is possible due to hopping, i.e. thermally assisted tunnelling of localized charge carriers [61, 62]. This effect is often observed, for example, in granular metal films or cermets with nanoparticles. Due to the small particle size, even small filling factors correspond to interparticle spacings of the order of 1 nm (see Eq. 1). Thus, far below f_c, where the particles would touch, a small dc conductivity $\sigma_{\text{dc}}^{\text{hop}} \ll \sigma_p$ is observed. It exceeds the value predicted by Eq. (9), but only a variation of the temperature allows the hopping process to be identified. The electrostatic charging energy, W, of a particle determines the temperature dependence of the effective conductivity and causes a decrease of σ_{dc} when the temperature is lowered. At high temperatures ($k_B T \geq W$)

$$\sigma_{\text{dc}} \propto \exp(-W/k_B T) \ , \tag{19}$$

while at low temperatures ($k_B T \ll W$)

$$\sigma_{\text{dc}} \propto \exp(T_0/T)^n \qquad 0.25 \leq n \leq 0.5 \ . \tag{20}$$

n depends on the transport mechanism (1D or 3D variable-range hopping) and on the material parameters, for example, on the temperature dependence of the charge carrier concentration ($n = 0.5$ is often observed in granular metals) [63–65]. The charging energy $W = e^2/2C$ of a spherical particle with diameter d is

$$W = \frac{1}{4\pi\varepsilon_0} \cdot \frac{e^2}{d} \cdot \frac{1}{\varepsilon_{\text{eff}}} \tag{21}$$

where ε_{eff} is the effective permittivity of the surrounding medium. For a nonpolar medium this is the static permittivity, while for a polar medium the polarization is to be taken into account: $1/\varepsilon_{\text{eff}} = 1/\varepsilon_\infty - 1/\varepsilon_s$ (the measured effective high- and low-frequency permittivities are a good approximation). Temperature-dependent broadband measurements allow the determination of W, ε_s and ε_∞, and thus of the size of the particles. This procedure also allows unknown localization centres to be identified. For example, in polyaniline, an intrinsically conducting polymer, hopping occurs between crystalline regions, i.e. so-called primary particles with $d = 8$ nm, while amorphous material forms the barriers [56].

In systems of ligand-stabilized nanoparticles the conductivity and its activation energy can be chemically tailored. Figure 9 displays measured activation energies of the dc conductivity (see Eq. 19) of Pd_{561} and Au_{55} nanoparticles connected by spacer molecules of different lengths (see Fig. 2) [16]. The longer the spacer molecules, the smaller the electronic transport between neighbouring particles. The system is disordered so the particles would touch at a filling factor $f_c \simeq 0.63$ [40]. According to Eq. (1) the interparticle spacing from 0.7 to 2.8 nm corresponds to filling factors in the range from

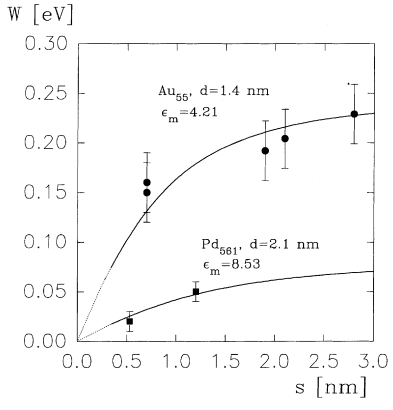

Fig. 9 Activation energy W vs. interparticle spacing s for ligand stabilized nanoparticles of Pd_{561} with $d = 2.1$ nm and Au_{55} with $d = 1.4$ nm (see Fig. 2). The *solid lines* represent calculations according to Eq. (21). ε_{eff} of the disordered system is given by Eq. (2) with x from Eq. (18) and f from Eq. (1) with $f_c = 0.63$. Only the constant ε_m has been fitted to the experimental data

32 to 2.3%. The solid lines are calculated from Eq. (21). Since the relaxation frequency of the interfacial process lies in the optical range, the effective permittivity can be considered as constant on the time scale of the hopping process. We use Eq. (2) with x from Eq. (18), which applies for disordered systems (for $f < 40\%$ this is equivalent to the random case, Eq. 17). The permittivity ε_m of the low-density nonpolar matrix, i.e. of ligand and spacer molecules, is the only free parameter fitted to the data. With decreasing s the filling factor and the effective static permittivity increase, i.e. the screening becomes more effective and the charging energy decreases. This continuous model ceases to be valid when s is close to the interatomic spacing (a few angstroms) and a continuous bulk phase forms. The hopping process breaks down and the intrinsic thermal activation of σ_p determines the observed temperature dependence.

Near the percolation threshold

At the percolation threshold, f_c, the first continuous conducting paths form and a strong increase of the dc conductivity is observed. Since the interparticle distances within a percolation path vanish, the capacitance diverges ($C \to \infty$) and so does ε_s [40]. This metallization transition occurs in ordered systems (see Eq. 13) as well as in disordered ones (inserting Eq. 18 in Eq. 2), but only in the limit of ideal conducting particles without any barriers or contact resistances in-between. In real systems a strong increase of ε_s is observed but the permittivity remains finite. There is a large number of statistical, geometrical and thermodynamical percolation models applicable to different materials (for a review see Ref. [51]). It is difficult to predict f_c in disordered nonrandom systems, where agglomeration may lead to the formation of long chains and thus to f_c values far below those expected for ordered or random systems.

For random systems percolation theory can be used near f_c, i.e. for $|f - f_c| \ll f_c$ [52]. The following assumptions have to be made:

1. $|\varepsilon_p| \gg |\varepsilon_m|$, i. e. the conductivity of the matrix is negligible, $\sigma_m \ll \sigma_p$. The small hopping conductivity below f_c is neglected as well.
2. There are no contact resistances or barriers between particles in contact.
3. Only low frequencies are considered, i. e. the range far below all polarization processes characterizing the microstructure of the system ($\nu \ll \nu_{\text{relax}}$, see Eq. 4).

In an intermediate frequency range $\nu_c \ll \nu \ll \nu_{\text{relax}}$, a scaling behaviour $\varepsilon'_{\text{eff}} \propto \omega^{-y}$, $\varepsilon''_{\text{eff}} \propto \omega^{x-1}$, and thus $\sigma_{\text{eff}} \propto \omega^x$ with $x + y \simeq 1$ is predicted [52, 53]. In the following treatment, we restrict ourselves to the quasi-static case $\nu \ll \nu_c$. Above f_c the effective dc conductivity is expected to scale as

$$\sigma_{\text{dc}}^{\text{eff}} = \sigma_0 (f - f_c)^t, \tag{22}$$

where t is the critical exponent. For the real part of ε_{eff}

$$\varepsilon'_s \propto \frac{\varepsilon'_m}{|f - f_c|^s} \tag{23}$$

holds for both $f < f_c$ and $f > f_c$. Of course, nonrandom systems will also show a strong increase of both the dc conductivity and the static permittivity. Nevertheless, deviations from Eqs. (22) and (23) become visible. The conductivity and the static dielectric constant of PAni/PETG blends are displayed in Fig. 10. Small amounts of the intrinsically conducting polyaniline were dispersed in amorphous insulating PETG, a modification of polyethylenterephtalate [56]. The conductivity of compressed pellets of PAni powder is $\sigma_{\text{PAni}} \geq 2000$ S/m. Above $f_c = 8.4\%$ the mixture shows dc conductivity and Eq. (22) holds with $t = 4.28$. Likewise, the static dielectric constant increases near f_c (see Eq. 23), but there is no symmetry around the percolation threshold. For $f > f_c$ the static permittivity remains large due to conduction current relaxation (see next section), an effect percolation theory cannot account for. The low percolation threshold shows that the conducting paths above f_c do not correspond to a random distribution (see the disordered case in Fig. 1).

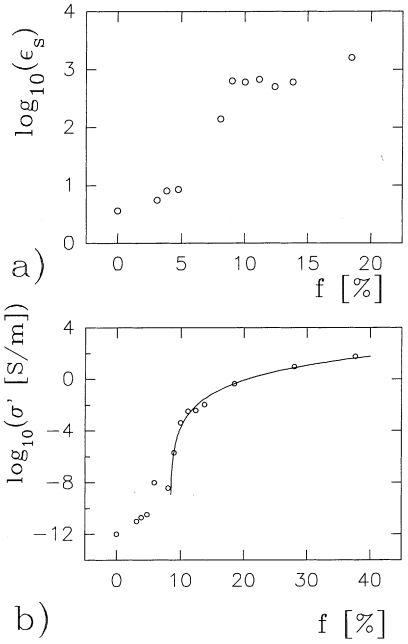

Fig. 10 a Static permittivity ε_s and **b** conductivity σ at 5 Hz vs filling factor f for intrinsically conducting polyaniline dispersed in insulating PETG. Above $f = 8.4\%$ dc conductivity occurs and σ (5 Hz)= σ_{dc} [56]. *Solid line*: fit according to Eq. (22) with $t = 4.28$

For the sake of completeness we mention the general effective media equation of McLachlan [54, 55] combining a mean-field mixture formula (neglecting higher multipoles) and Eq. (22) in order to overcome the respective restrictions $f \ll 1$ and $f \simeq f_c$. Due to adjustable parameters (exponent t, f_c) this phenomenological equation can be used to fit a large amount of experimental data but it is not an exact solution of the effective medium problem.

Conduction current relaxation

Conducting paths form across the sample either above f_c or even below when hopping occurs. Nanodispersion becomes a heterogeneous conductor and current flow in paths which are not parallel to the electric field can give rise to a partial interfacial polarization. Charge carriers accumulate at the boundaries of less-conducting regions, creating dipolar polarization and thus a frequency-dependent permittivity [57]. The dc conductivity is determined by the paths with the least resistance.

In a first step we consider an ordered system of inclined insulating and conducting layers (see Fig. 11a). The latter ones are thought to consist of particles in contact and to exhibit a conductivity $\sigma_{\text{path}} < \sigma_p$. Such a system can be described by a superposition of a series and a parallel circuit (see Fig. 6b) [58, 59]:

$$\varepsilon_{\text{eff}}(\omega) = \cos^2\theta \cdot \varepsilon_{\text{series}} + \sin^2\theta \cdot \varepsilon_{\parallel} \ . \tag{24}$$

where $\varepsilon_{\parallel} = (1-f)\varepsilon'_m + f[\varepsilon'_{\text{path}} - i\sigma_{\text{path}}/(\varepsilon_0\omega)]$ and $\varepsilon^{-1}_{\text{series}} = (1-f)/\varepsilon'_m + f/[\varepsilon'_{\text{path}} - i\sigma_{\text{path}}/(\varepsilon_0\omega)]$. After a simple calculation Eq. (24) can be written as

$$\varepsilon_{\text{eff}}(\omega) = \varepsilon_{\text{hf}} + \frac{\Delta\varepsilon}{1+i\omega\tau} - i\frac{\sigma_{\text{dc}}}{\varepsilon_0\omega} \ , \tag{25}$$

where ε_{hf} denotes the effective permittivity at high frequencies, $\Delta\varepsilon \propto \cos^2\theta$, and $\sigma_{\text{dc}} = f\sigma_{\text{path}}\sin^2\theta$. $\tau \propto 1/\sigma_{\text{path}}$ is independent of θ. The characteristic relation between relaxation strength, relaxation time and effective conductivity is [59]

$$\sigma_{\text{dc}} = \frac{\varepsilon_0\Delta\varepsilon}{\tau}p \ , \tag{26}$$

with $p = \tan^2\theta[1 + (1-f)(\varepsilon'_{\text{path}}/\varepsilon'_m - 1)]^2$. This so-called conduction current relaxation occurs for all inclination angles $0 < \theta < \pi/2$.

More realistic microstructures are better described as inhomogeneous conductors with curved paths (see Fig. 11b and c for the ordered and nonordered case). An extension of the above model revealed that Eq. (26) remains valid, while the shape of the polarization process is broadened [60]. Dyre [57] reaches the same conclusion in his "macroscopic" model, where he describes an inhomogeneous solid with spatially randomly varying conductivities. Referring to Fig. 11b and c we can consider p as a measure for an averaged deviation between current flow and external electric field, for example, due to zigzag paths: $p \propto \tan^2\theta = <\tan^2(\frac{\pi}{2} - \arccos(\mathbf{EI}/(EI)))>_{\text{avg}}$, so its actual value depends on details of the path topology. $p \simeq 1$ has been found for many materials and in this case Eq. (26) is also called the Barton-Nakajima-Namikawa relation. In general, a relaxation strength $\Delta\varepsilon \gg 1$ hints at a transport mechanism on a larger nonatomic scale. The permittivity of PAni/PETG blends (an aggregate topology) where $\Delta\varepsilon \simeq 500$ is displayed in Fig. 12a. Equation 26 holds for all filling factors $f > f_c \simeq 8.4\%$ and for temperatures from $T = 101$–297 K (see Fig. 12b). Experiment yields $p \simeq 0.05 \ll 1$, possibly due to the above-mentioned nonrandom distribution of conducting paths.

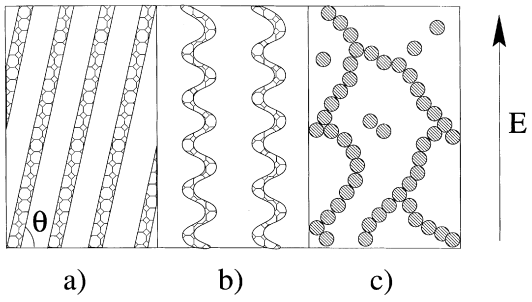

Fig. 11 **a** An ordered system, where the particles form inclined layers with $\sigma_{\text{path}} \leq \sigma_p$. **b** Ordered and **c** nonordered curved paths of nanoparticles

Since the conducting paths are composed of single particles (Fig. 11), contact resistances or barriers can lead to an additional interfacial polarization (Eq. 4). The relaxation frequency and the effective relaxation strength depend on the fraction of particles incorporated in paths and their spatial distribution. The dielectric functions of both processes, i.e. of a complete and of a partial interfacial polarization, are similar in shape (Eqs. 4 and 25) but the relaxation frequencies differ (see Eqs. 10 and 26). The conduction current relaxation is governed by the effective conductivity, i.e. $\nu_{\text{relax}} \propto \sigma_{\text{dc}} \propto \sigma_{\text{path}}$, where σ_{path} depends on the contact resistances between the particles. With increasing filling factor additional percolation paths form, σ_{dc} increases strongly and the relaxation process is shifted towards higher frequencies (the factor p in Eq. 26 is constant as long as the topology of the system does not change with increasing f). The relaxation frequency of a Maxwell-Wagner-Sillars process is determined by the particle conductivity $\nu_{\text{relax}} \propto \sigma_p$. It is much less affected by an increase of f, since the existence of additional paths does not change the distances between the particles in a percolation path (see Eq. 8 with $f \to f_{\text{path}} = \text{const.}$, $\varepsilon'_m \to \varepsilon'_{\text{barrier}}$ and $\sigma_m \to \sigma_{\text{barrier}}$). In the following section we shall show how temperature-dependent measurements can help to distinguish the two processes at constant f.

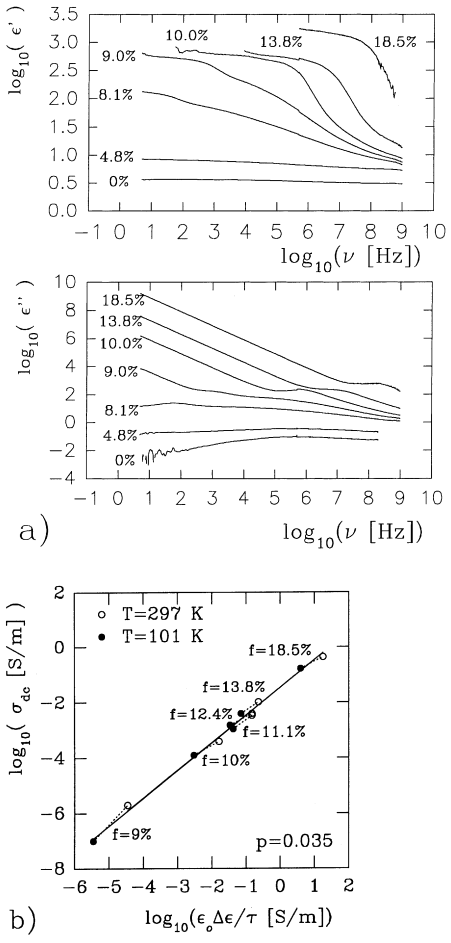

Fig. 12 **a** Permittivity $\varepsilon_{\text{eff}} = \varepsilon' - i\varepsilon''$ of a PAni/PETG blend vs frequency ν in a double-log plot. Above the critical filling factor $f_c = 8.4\%$ dc conductivity is observed, i.e. $\varepsilon'' \simeq \sigma_{\text{dc}}/(\varepsilon_0\omega)$ at low frequencies. **b** Dc conductivity σ_{dc} vs. relaxation strength over relaxation time, $\varepsilon_0\Delta\varepsilon/\tau$, for different Pani/PETG blends ($f > f_c$) at $T = 297$ K (*open circles*) and $T = 101$ K (*filled circles*). The linear relation, Eq. (26) is observed

Microstructure and transport mechanism

In this section we shall give an example showing that both conduction current relaxation and Maxwell-Wagner-Sillars polarization can occur in one and the same system. The permittivity of a sintered SiC ceramic (for details we refer to Ref. [64]) is shown in Fig. 13. Due to boron doping of 7.5 at% the material exhibits dc conductivity. The ceramics consist of crystalline grains (1–10 μm) separated by thin amorphous grain boundaries acting as a less conducting matrix. The microstructure shown in Fig. 14 is that of a matrix-inclusion system with $f \simeq 0.97$ (see also Fig. 1 at high f). Since the sample preparation (sintering, milling, etc.) creates lattice and surface defects, the respective permittivities and conductivities of both the particles and the matrix are unknown. At room temperature two relaxations are observed (see Fig. 13), one near 1 kHz and a second one near 10 MHz:

$$\varepsilon_{\text{eff}}(\omega, T) = \varepsilon_\infty + \frac{\Delta\varepsilon_1}{1 + (i\omega\tau_1)^{1-\alpha_1}} + \frac{\Delta\varepsilon_2}{1 + (i\omega\tau_2)^{1-\alpha_2}} - i\frac{\sigma_{\text{dc}}}{\varepsilon_0\omega} \quad . \tag{27}$$

The exponents $\alpha_1 = 0.5$ and $\alpha_2 = 0.1$ take the broadening of the relaxations into account ($\alpha = 0$ corresponds to the Debye-form of Eq. 4 or Eq. 25). With decreasing temperature the dc conductivity decreases and both processes are shifted towards lower frequencies. Huge relaxation strengths $\Delta\varepsilon \gg 100$ are observed, indicating interfacial polarization mechanisms. For both procceses

$$\sigma_{\text{dc}}(T) = \alpha\frac{\varepsilon_0\Delta\varepsilon(T)}{\tau(T)} \tag{28}$$

holds (see Fig. 15). The low frequency process with $\alpha = 1$ corresponds to a conduction current relaxation (see Eq. 26 with $p = 1$). However, there are also grain

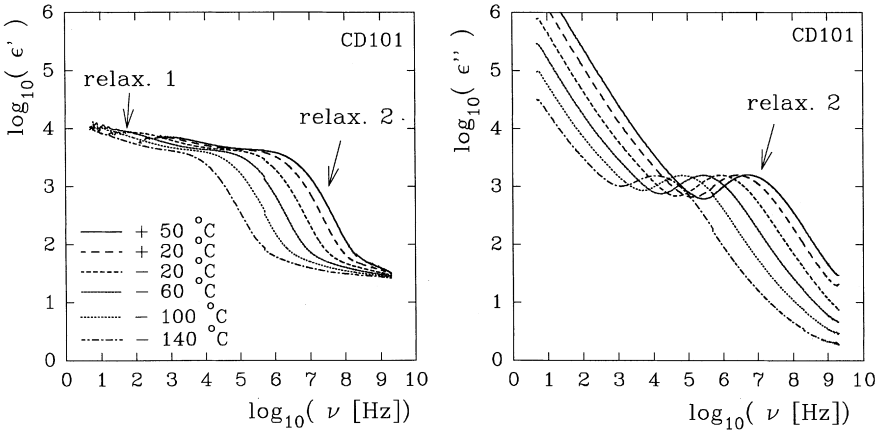

Fig. 13 Permittivity $\varepsilon_{\text{eff}} = \varepsilon' - i\varepsilon''$ of boron-doped SiC ceramics at different temperatures vs. frequency ν in a double-log plot [64]

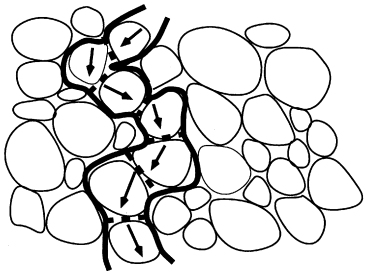

Fig. 14 Current paths in a SiC ceramics. The *thick solid lines* indicate grain boundaries responsible for the conduction current relaxation and the *dashed lines* show the boundaries causing Maxwell-Wagner-Sillars interfacial polarization at high frequencies [64]

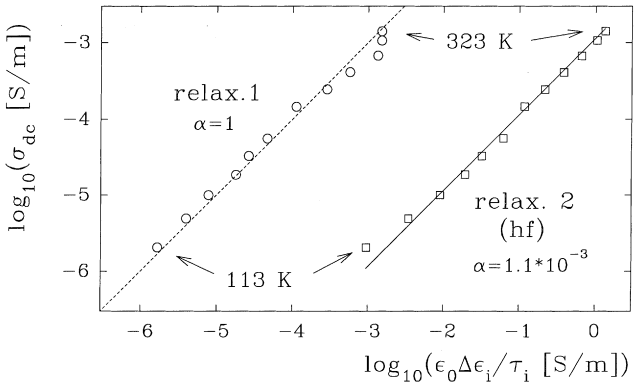

Fig. 15 dc conductivity σ_{dc} vs. relaxation strength over a relaxation time, $\varepsilon_0\Delta\varepsilon/\tau$, for the two processes shown in Fig. 13

boundaries inside the current paths (dashed lines in Fig. 14). They give rise to an interfacial polarization process. This occurs at higher frequencies than the conduction current relaxation, since the conductivity of the crystalline grains is higher than that of the current paths which are made up of grains and grain boundaries (see Eqs. 10 and 26). In the limit $f \to 1$ Eqs. (4)–(10) are good approximations, since the current flow in the paths with the least resistance can be approximated by a series circuit. Equation (28) equals Eq. (10) with $\alpha = \gamma\sigma_{dc}/(f\sigma_p) \ll 1$, which is in fact observed for the high-frequency process ($\alpha = 1.1 \times 10^{-3}$, see Fig. 15). Both grains and boundaries consist of SiC, so α does not change with temperature and $\gamma \simeq 1$ ($\varepsilon'_p \simeq \varepsilon'_m$) independent of the exact value of the depolarization factor A (see Eq. 10). At 20 °C $\sigma_{dc} = 6.7 \times 10^{-4}$ S/m is observed and thus $\sigma_p(20\,°C) = \sigma_{dc}\gamma/(\alpha f) = 0.63$ S/m. The conductivity of the crystalline grains is three orders of magnitude higher than the measured effective one. Lowering the boron doping by a factor of 2 and repeating the above analysis yields a particle conductivity reduced by the same factor and confirms the above analysis. Although the dc conductivity of the ceramics is governed by the matrix material, broadband temperature-dependent spectroscopy from dc to 1 GHz enables us to determine the conductivity of the particles.

Conclusion

We have described various preparation techniques for nanodispersions and their capability to control microstructure. The degree of order depends on the distribution of particle sizes and interparticle spacings, and this is reflected in the dielectric response of the composites. While it is possible to calculate ε_{eff} for a given particle arrangement, the main challenge is the solution of the inverse problem. An insight into the spatial distribution and single particle properties is possible when the strong frequency and temperature dependence of the DF is taken into account, i.e. via the analysis of charge transport and polarization processes. Therefore, temperature-dependent broadband dielectric spectroscopy can be used as a nondestructive method to investigate microstructure on the nanometer scale.

Acknowledgements We are grateful to G. Nimtz, G. Schön and A. Spanoudaki for stimulating discussions. This work was financially supported by the "Bundesminister für Bildung, Wissenschaft, Forschung und Technologie" (BMBF) under Contract No. 03N1012A7 as well as by the "Deutsche Forschungsgemeinschaft" (DFG project Ni 149/22-2).

References

1. Schmid G (1992) Chem Rev 92: 1709
2. Schmid G (ed) (1994) Clusters and colloids. VCH, Weinheim
3. Schön G, Simon U (1995) Colloid Polym Sci 273: 101; 273: 202
4. Weller H (1993) Angew Chem 105: 43; (1996) Angew Chem 108: 1159
5. Halperin WP (1986) Rev Mod Phys 58: 533
6. van Kempen H, Dubois JGA, Gerritsen JW, Schmid G (1995) Physica B 204: 51
7. Brus LE (1983) J Chem Phys 79: 5566
8. Alivisatos AP (1996) J Phys Chem 100: 13226
9. Schmid G, Morun B, Malm JO (1989) Angew Chem Int Ed Engl 28: 778; Schmid G, Lehnert A (1989) Angew Chem Int Ed Engl 28: 780
10. Fenske D, Krautscheid H (1990) Angew Chem Int Ed Engl 29: 1452; Dehnen S, Fenske D (1994) Angew Chem Int Ed Engl 33: 2287
11. Henglein A, Lille J (1981) J Phys Chem 85: 1246; Ershov BG, Janata E, Michaelis M, Henglein A (1991) J Phys Chem 95: 8996; Henglein A, Guttierez M, Janata E, Ershov BG (1992) J Phys Chem 96: 4598
12. Bradley JS (1994) In: Schmid G (ed) Clusters and colloids. VCH, Weinheim pp 549–537
13. Voßmeier T, Reck G, Katsikas L, Haupt ETK, Schulz B, Weller H (1995) Science 267: 1476; Voßmeier T, Reck G, Schulz B, Katsikas L, Weller H (1995) J Am Chem Soc 117: 12881
14. van Staveren MPJ, Brom HB, de Jongh LJ (1991) Phys Rep 208: 1
15. Krauthäuser HG, Pelster R, Simon U, (unpublished results of SAXS and dielectric experiments)

16. Simon U, Flesch R, Wiggers H, Schön G, Schmid G (1998) J Mater Chem 8: 517; Schmid G and Chi LF (1998) Adv Mater 10: 515
17. Brust M, Bethell D, Schiffrin DJ, Kiely CJ (1995) Adv Mater 7: 795
18. Spatz JP, Roescher A, Sheiko S, Krausch G, Möller M (1995) Adv Mater 7: 731; Spatz JP, Roescher A, Möller M (1996) Adv Mater 8: 337
19. Ozin GA (1992) Adv Mater 10: 612; (1994) In: Interante L (ed) Adv Chem Ser, ACS, Washington DC, pp 103–141
20. Exner D, Jaeger NI, Kleine A, Schulz-Ekloff G (1988) J Chem Soc Faraday Trans 184: 4097
21. Sradanov VI, Haug K, Metiu H, Stucky GD (1992) J Phys Chem 96: 9039
22. Herron N, Wang Y, Eddy MM, Stucky GD, Cox D, Möller K, Bein T (1989) J Am Chem Soc 111: 530
23. Jacobs PA, Jaeger NI, Jiru P, Schulz-Ekloff G (eds) (1982) Metal microstructures in zeolites. Elsevier, Amsterdam
24. Wark M, Kessler H, Schulz-Ekloff G (1997) Microporous Mater 8: 241
25. Schwenn HJ, Wark M, Schulz-Ekloff G, Wiggers H, Simon U (1997) Colloid Polym Sci 275: 91
26. Wiggers H, Simon U, Schön G (1998) Solid State Ionics 107: 111
27. Davis SC, Klabunde K (1982) J Chem Rev 82: 153
28. Lamber R, Baalmann A, Jaeger NI, Schulz-Ekloff G, Wetjen S (1994) Adv Mater 6: 223
29. Janes DB, Kolagunta VR, Osifchin RG, Bielefeld JD, Andres RP, Henderson JI, Kubiak CP (1995) Superlattices Microstruct 18: 275; Andres RP, Bein Th, Dorogi M, Feng S, Henderson JI, Kubiak CP, Mahoney W, Osifchin RG, Reifenberger R (1996) Science 272: 1323
30. van Beek LKH (1967) In: Birks JB (ed) Progress in dielectrics, vol 7. Heywood, London, pp 69–114
31. Dukhin SS (1971) In: Matijevic E (ed) Surface and colloid science, vol 3. Interscience, New York, pp 83–165
32. Cini M and Ascarelli P (1974) J Phys F 4: 1998
33. McKenzie DR, McPhedran RC (1977) Nature 265: 128; (1978) Proc R Soc Lond Ser A 359: 45
34. Doyle WT (1978) J Appl Phys 49: 795
35. McKenzie DR, McPhedran RC, Derrick GH (1978) Proc R Soc Lond Ser A 362: 211
36. Sareni B, Krähenbühl L, Beroual A, Brosseau C (1996) J Appl Phys 80: 1688; 80: 4560
37. Nicorovici NA, McPhedran RC (1996) Phys Rev E 54: 1945
38. Bánhegyi G (1988) Colloid Polym Sci 266: 11
39. Moenecke J (1989) Phys Status Solids B 154: 805
40. Doyle WT, Jacobs IS (1990) Phys Rev B 42: 9319
41. Grunow V (1994) Diploma thesis, University of Cologne
42. Pelster R, Kops A, Nimtz G, Enders A, Kietzmann H, Pissis P, Kyritsis A, Woermann D (1993) Ber Bunsenges Phys Chem 97: 666
43. Fu L, Resca L (1993) Phys Rev B 47: 16194
44. Fu L, Macedo PB, Resca L (1993) Phys Rev B 47: 13818
45. Sheu S, Kumar S, Cukier RI (1990) Phys Rev B 42: 1431
46. Stölzle S, Enders A, Nimtz G (1992) J Phys I France 2: 401
47. Stölzle S, Enders A, Nimtz G (1992) J Phys I France 2: 1765
48. Pelster R (to be published)
49. Schwenn HJ, Wark M, Schulz-Ekloff G, Wiggers H, Simon U (1997) Colloid Polym Sci 275: 91
50. Pelster R, Marquardt P, Nimtz G, Enders A, Eifert H, Friederich K, Petzoldt F (1992) Phys Rev B 45: 8929
51. Lux F (1993) J Mater Sci 28: 285
52. Shalaev VM (1996) Phys Rep 272: 61
53. Chakrabarty RK, Bardhan KK, Basu A (1993) J Phys Condens Matter 5: 2377
54. McLachlan DS (1989) Solid State Commun 72: 831
55. Michels MAJ (1992) J Phys Condens Matter 4: 3961
56. Pelster R, Nimtz G, Weßling B (1994) Phys Rev B 49: 12718
57. Dyre JC (1993) Phys Rev B 48: 12511
58. Yamamoto K, Namikawa H (1988) Jpn J Appl Phys 27: 1845
59. Yamamoto K, Namikawa H (1989) Jpn J Appl Phys 28: 2523
60. Yamamoto K, Namikawa H (1992) Jpn J Appl Phys 31: 3619
61. Pollak M, Adkins CJ (1992) Phil Mag B 65: 885
62. Adkins CJ (1992) J Phys C 15: 7143
63. Li Q, Cruz L, Phillips P (1993) Phys Rev B 47: 1840
64. Schroeder A, Pelster R, Grunow V, Lennartz W, Nimtz G, Friedrich K (1996) J Appl Phys 80: 2260
65. Sheng P, Abeles B (1972) Phys Rev B 28: 34
66. Flesch R (1997) PhD thesis, University of Essen